Physico-Geometrical Mechanism and Overall Kinetics of Thermally Induced Oxidative Decomposition of Tin(II) Oxalate in Air: Formation Process of Microstructural Tin(IV) Oxide

Suguru Kitabayashi and Nobuyoshi Koga*

Department of Science Education, Graduate School of Education, Hiroshima University, 1-1-1 Kagamiyama, Higashi-Hiroshima 739-8524, Japan.
*Corresponding author, e-mail: nkoga@hiroshima-u.ac.jp

S1. Changes in the samples during the reaction

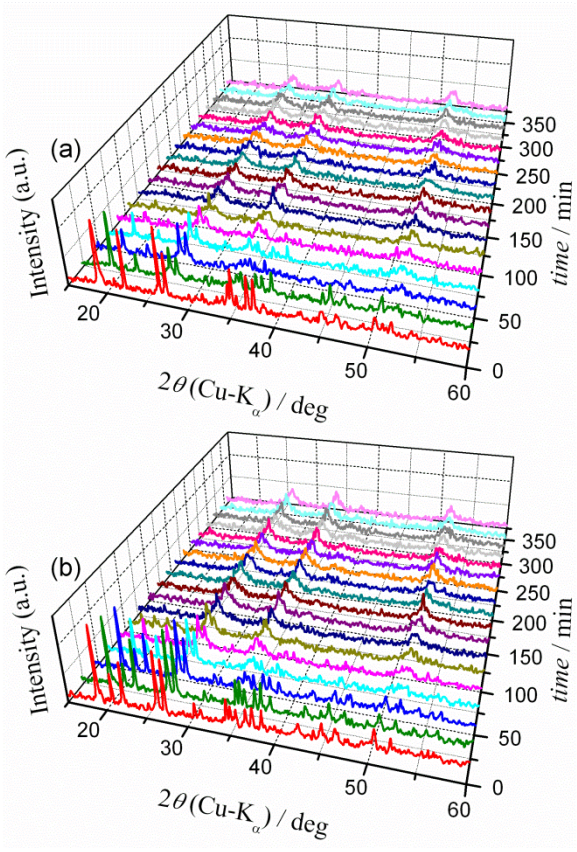

Figure S1. Changes in XRD patterns of the samples during isothermal heating in flowing air (100 cm^3 min^{-1}): (a) W50 at 563 K; and (b) E50 at 553 K.

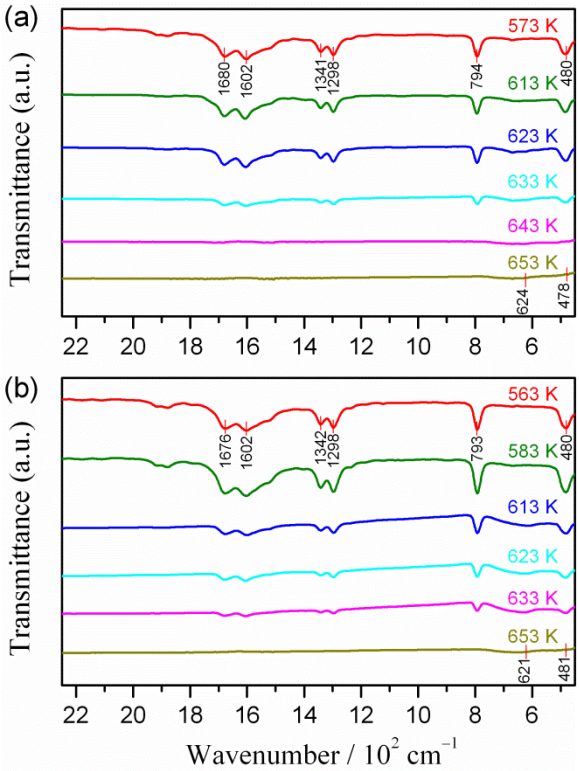

Figure S2. Changes in FTIR spectra of the samples heated to different temperatures at β = 10 K min^{-1} in flowing air (80 cm^3 min^{-1}): (a) W50 and (b) E50.

S2. Initial kinetic parameters for the kinetic deconvolution of the reaction of W50

For rapid estimation of the contribution, c_i, of the constitutive reaction steps in the overall reaction, derivative TG (DTG) curves recorded under isothermal and linear nonisothermal conditions were resolved by a statistical method using the PeakFit Ver.4.2 software. The Weibull function (eq S1) was assumed for the estimation because of the satisfactory fitting observed empirically for multi-step reactions in the solid-state.[S1-S5]

$$y = a_0\left(\frac{a_3-1}{a_3}\right)^{\frac{1-a_3}{a_3}}\left(\frac{x-a_1}{a_2}+\left(\frac{a_3-1}{a_3}\right)^{\frac{1}{a_3}}\right)^{a_3-1} \times \exp\left[-\left(\frac{x-a_1}{a_2}+\left(\frac{a_3-1}{a_3}\right)^{\frac{1}{a_3}}\right)^{a_3}+\frac{a_3-1}{a_3}\right] \quad \text{(S1)}$$

where a_0–a_3 are the amplitude, center, width, and shape, respectively.

Typical results of the mathematical deconvolution of DTG curves for the overall reaction of W50 under isothermal and linear nonisothermal conditions are shown in Figure S3. The overall reaction was satisfactorily resolved into two reaction steps under isothermal conditions and three reaction steps under linear nonisothermal conditions. The estimated contributions of each constitutive reaction step, c_i, did not change depending on the reaction temperature under isothermal conditions. The values of c_i of the second and third reaction steps tended to vary depending on β under linear nonisothermal conditions. The average c_i are listed in Table S1.

Figures S4 and S5 show the kinetic curves for each constitutive reaction step, i, resolved by the mathematical deconvolution for the reaction under isothermal and linear nonisothermal conditions, respectively. From the series of kinetic curves for each reaction step, the apparent values of E_a at different α were determined by Friedman plots[S6] on the basis of eq 2 in the main text. Figure S6 shows the apparent E_a for each reaction step under isothermal and linear nonisothermal conditions. For each reaction step, the values of E_a at different α are approximately constant over the course of the reaction step. The averaged $E_{a,i}$ of the respective reaction steps ($0.1 \leq \alpha \leq 0.9$) are listed in Table S1.

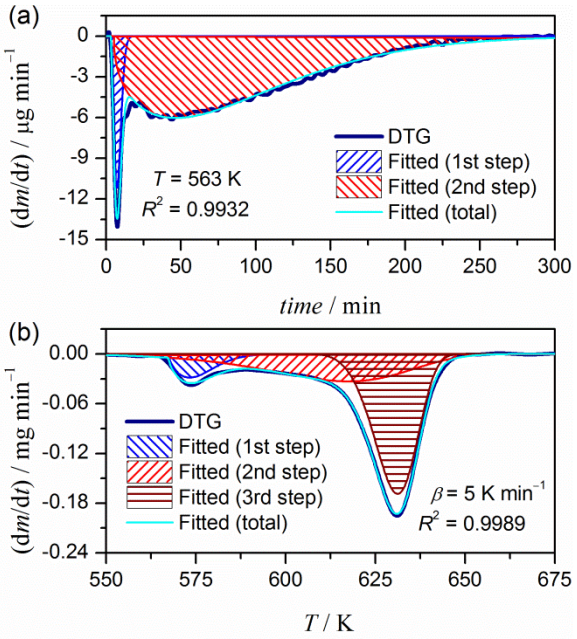

Figure S3. Typical results of the mathematical deconvolution of DTG curves for the reaction of W50: (a) isothermal and (b) linear nonisothermal conditions.

Table S1. The contribution, c_i, and the average $E_{a,i}$ of each reaction step for the reaction of W50

Condition	Step, *i*	c_i	$E_{a,i}$ / kJ mol^{-1}[a]
Isothermal	1	0.08 ± 0.02	225.5 ± 3.0
	2	0.92 ± 0.02	137.2 ± 5.7
Nonisothermal	1	0.07 ± 0.01	247.3 ± 7.2
	2	0.43 ± 0.09	123.5 ± 2.7
	3	0.50 ± 0.09	229.9 ± 9.3

[a] Averaged over $0.1 \leq \alpha \leq 0.9$.

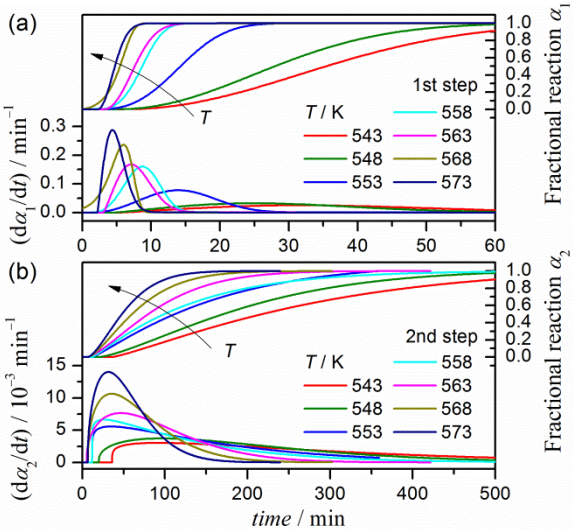

Figure S4. Kinetic curves for the respective reaction steps resolved by the mathematical deconvolution of the overall reaction of W50 under isothermal conditions at different temperatures: (a) 1st and (b) 2nd reaction steps.

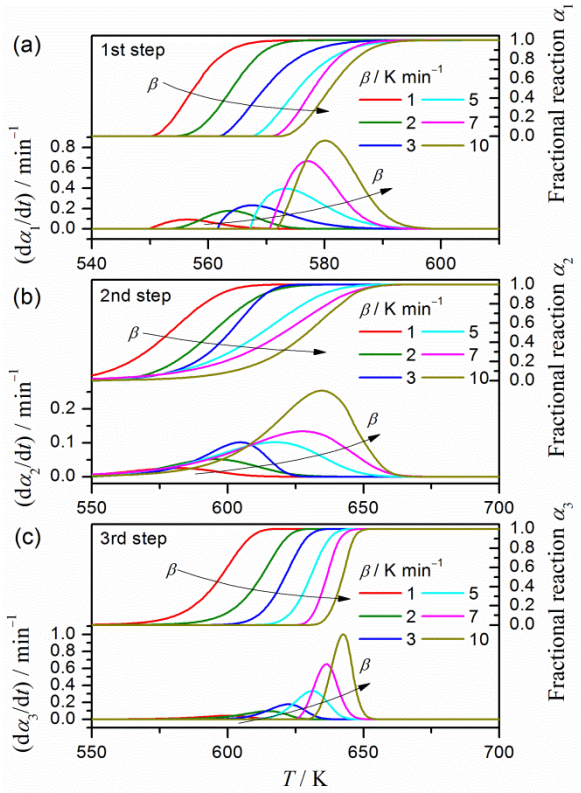

Figure S5. Kinetic curves for the respective reaction steps resolved by the mathematical deconvolution of the overall reaction of W50 under linear nonisothermal conditions at different β: (a) 1st, (b) 2nd, and (c) 3rd reaction steps.

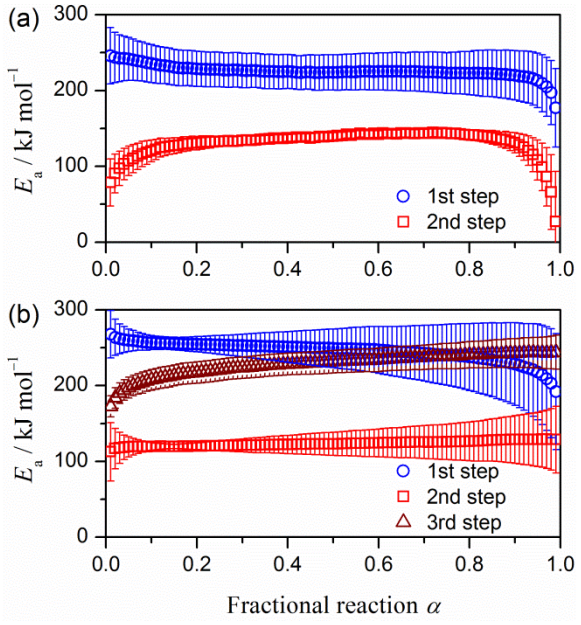

Figure S6. The values of $E_{a,i}$ at different α determined by the Friedman plots for the series of kinetic curves of each reaction step of W50 resolved by mathematical deconvolution: (a) isothermal and (b) linear nonisothermal conditions.

The values of c_i listed in Table S1 were used as the initial values for the kinetic deconvolution of the reaction. For the kinetic deconvolution of the reaction under isothermal conditions, the first order reaction expressed using SB(0,1,0) was assumed for all the reaction steps and the initial rate constants, k_i, of the respective reaction steps at each reaction temperature in eq 3 in the main text were estimated with reference to the apparent $E_{a,i}$ listed in Table S1.[S7,S8] Similarly, for the kinetic deconvolution of the reaction under linear nonisothermal conditions based on eq 4, the values of c_i and $E_{a,i}$ listed in Table S1 were used as the initial values. After setting the first order reaction SB(0,1,0) for all the reaction steps, the order of the initial A_i values were determined graphically by comparing the calculated kinetic curve and experimental kinetic curve.[S5,S7-S13]

After setting all the initial kinetic parameters in eqs 3 and 4 in the main text, the kinetic deconvolution operation was performed and all the kinetic parameters were optimized.

S3. Initial kinetic parameters for the kinetic deconvolution of the reaction of E50

The same procedure for determining the initial kinetic parameters for the kinetic deconvolution was employed for the reactions of W50 and E50. For the reaction of E50, the overall reaction was resolved into two reaction steps irrespective of isothermal and linear nonisothermal conditions (Figure S7).

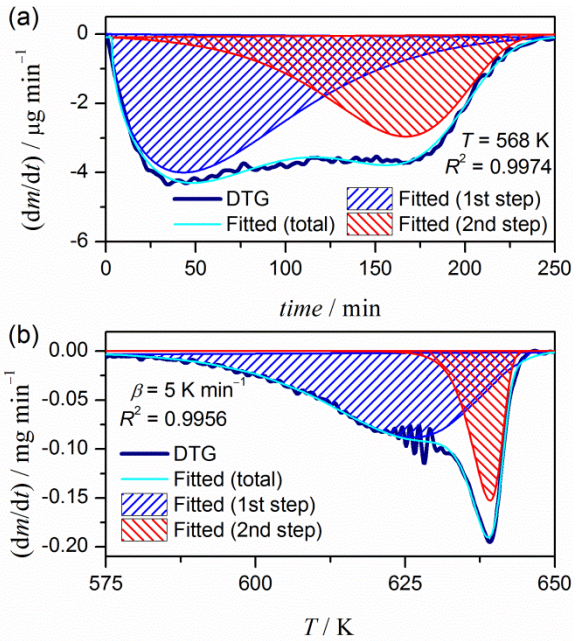

Figure S7. Typical results of the mathematical deconvolution of DTG curves for the reaction of E50: (a) isothermal and (b) linear nonisothermal conditions.

The values of c_i estimated by the mathematical deconvolution are approximately constant in the reactions under both isothermal and linear nonisothermal conditions. The average c_i of each reaction step are listed in Table S2. The series of kinetic curves of each constitutive reaction step of E50 under isothermal and linear nonisothermal conditions, resolved by mathematical deconvolution, are shown in Figures S8 and S9, respectively. The values of $E_{a,i}$ at different α determined from the Friedman plots for the respective series of kinetic curves shown in Figures S8 and S9 are approximately constant over the course of each reaction step (Figure S10), giving the average value listed in Table S2. The average values of c_i and $E_{a,i}$ of the respective reaction steps were used for setting the initial kinetic parameters for the kinetic deconvolution operations on the basis of eqs 3 and 4 in the main text as was done for W50.

Table S2. The contributions, c_i, and the average $E_{a,i}$ of each reaction step of the reaction of E50

Condition	Step, *i*	c_i	$E_{a,i}$ / kJ mol^{-1},[a]
Isothermal	1	0.60 ± 0.02	136.9 ± 6.5
	2	0.40 ± 0.02	183.5 ± 3.0
Nonisothermal	1	0.74 ± 0.04	170.0 ± 5.7
	2	0.26 ± 0.04	196.8 ± 3.2

[a] Averaged over $0.1 \le \alpha \le 0.9$.

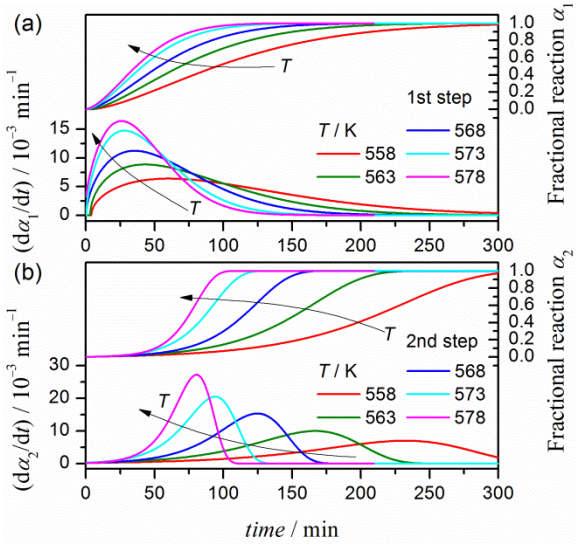

Figure S8. Kinetic curves for the respective reaction steps resolved by the mathematical deconvolution of the overall reaction of E50 under isothermal conditions at different temperatures: (a) 1st and (b) 2nd reaction steps.

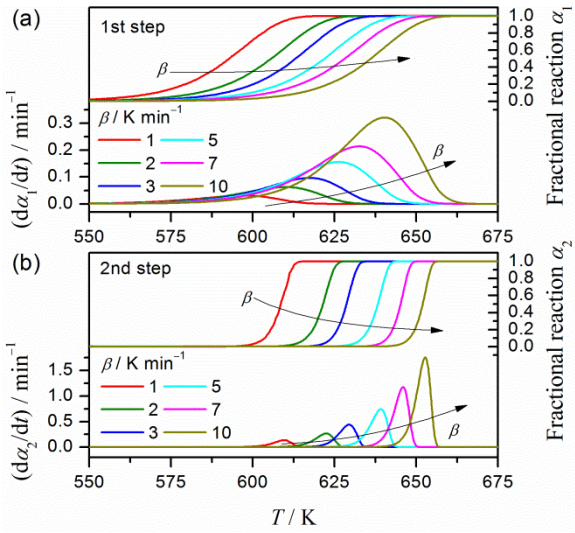

Figure S9. Kinetic curves for the respective reaction steps resolved by the mathematical deconvolution of the overall reaction of E50 under linear nonisothermal conditions at different β. (a) 1st and (b) 2nd reaction steps.

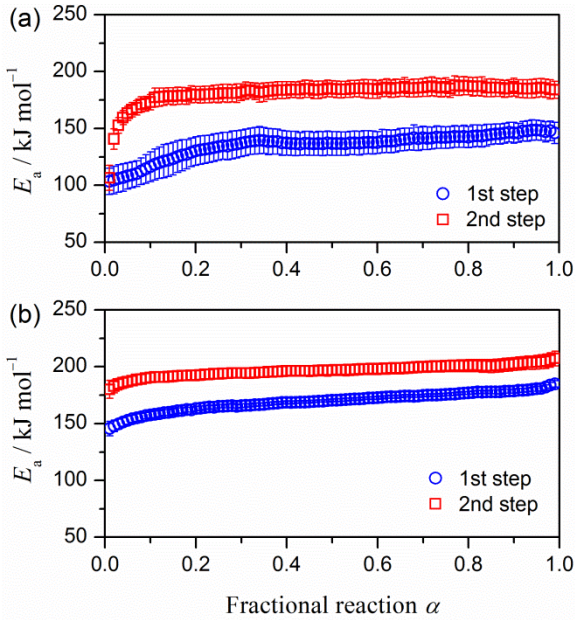

Figure S10. The values of $E_{a,i}$ at different α determined by the Friedman plots for the series of kinetic curves for each reaction step of E50 resolved by mathematical deconvolution: (a) isothermal and (b) linear nonisothermal conditions.

References

(1) Cai, J.; Liu, R. Weibull Mixture Model for Modeling Nonisothermal Kinetics of Thermally Stimulated Solid-State Reactions: Application to Simulated and Real Kinetic Conversion Data. *J. Phys.Chem. B* **2007**, *111*, 10681-10686.

(2) Cai, J.; Alimujiang, S. Kinetic Analysis of Wheat Straw Oxidative Pyrolysis Using Thermogravimetric Analysis: Statistical Description and Isoconversional Kinetic Analysis. *Ind. Eng. Chem. Res.* **2009**, *48*,

619-624.
(3) Janković, B.; Adnađević, B.; Kolar-Anić, L.; Smičiklas, I. The Non-Isothermal Thermogravimetric Tests of Animal Bones Combustion. Part II. Statistical Analysis: Application of the Weibull Mixture Model. *Thermochim. Acta* **2010**, *505*, 98-105.
(4) Perejon, A.; Sanchez-Jimenez, P. E.; Criado, J. M.; Perez-Maqueda, L. A. Kinetic Analysis of Complex Solid-State Reactions. A New Deconvolution Procedure. *J. Phys. Chem. B* **2011**, *115*, 1780-1791.
(5) Koga, N.; Goshi, Y.; Yamada, S.; Pérez-Maqueda, L. A. Kinetic Approach to Partially Overlapped Thermal Decomposition Processes. *J. Therm. Anal. Calorim.* **2013**, *111*, 1463-1474.
(6) Friedman, H. L. Kinetics of Thermal Degradation of Cha-Forming Plastics from Thermogravimetry, Application to a Phenolic Plastic. *J. Polym. Sci. C* **1964**, *6*, 183-195.
(7) Koga, N.; Yamada, S.; Kimura, T. Thermal Decomposition of Silver Carbonate: Phenomenology and Physicogeometrical Kinetics. *J. Phys. Chem. C* **2013**, *117*, 326-336.
(8) Wada, T.; Koga, N. Kinetics and Mechanism of the Thermal Decomposition of Sodium Percarbonate: Role of the Surface Product Layer. *J. Phys. Chem. A* **2013**, *117*, 1880-1889.
(9) Koga, N.; Suzuki, Y.; Tatsuoka, T. Thermal Dehydration of Magnesium Acetate Tetrahydrate: Formation and In Situ Crystallization of Anhydrous Glass. *J. Phys. Chem. B* **2012**, *116*, 14477-14486.
(10) Koga, N.; Kasahara, D.; Kimura, T. Aragonite Crystal Growth and Solid-State Aragonite–Calcite Transformation: A Physico–Geometrical Relationship via Thermal Dehydration of Included Water. *Cryst. Growth Des.* **2013**, *13*, 2238-2246.
(11) Koga, N.; Nishikawa, K. Mutual Relationship between Solid-State Aragonite–Calcite Transformation and Thermal Dehydration of Included Water in Coral Aragonite. *Cryst. Growth Des.* **2014**, *14*, 879-887.
(12) Noda, Y.; Koga, N. Phenomenological Kinetics of the Carbonation Reaction of Lithium Hydroxide Monohydrate: Role of Surface Product Layer and Possible Existence of a Liquid Phase. *J. Phys. Chem. C* **2014**, *118*, 5424-5436.
(13) Yoshikawa, M.; Yamada, S.; Koga, N. Phenomenological Interpretation of The Multistep Thermal Decomposition of Silver Carbonate to Form Silver Metal. *J. Phys. Chem. C* **2014**, *118*, 8059-8070.